ELSEVIER

Available online at www.sciencedirect.com

SCIENCE DIRECT®

Physica B 340–342 (2003) 933–938

PHYSICA B

www.elsevier.com/locate/physb

EPR and electrical studies of native point defects in $ZnSiP_2$ semiconductors

W. Gehlhoff[a,*], D. Azamat[a,1], A. Krtschil[b], A. Hoffmann[a], A. Krost[b]

[a] Institute for Solid State Physics, Technical University Berlin, Hardenbergstr 36, Berlin D-10623, Germany

[b] Institute of Experimental Physics, Otto-von-Guericke-University Magdeburg, P.O. Box 4120, Magdeburg D-39016, Germany

Abstract

We present the first detection of native defects in $ZnSiP_2$. Similar to p-type $ZnGeP_2$, the EPR spectra of the zinc vacancy V_{Zn}^-, the phosphorus vacancy V_P^0, as well as of group IV anti-site $Si_{Zn}^+(Ge_{Zn}^+)$ could be proved. The influence of the group IV-ions on the bonding behavior for the different lattice sites is reflected in the differences of the EPR parameters in both lattices. In both materials, V_P^0 could be observed only by photo-excitation, whereas the silicon anti-site Si_{Zn}^+ was detectable also in the dark contrary to Ge_{Zn}^+. This is connected with the shift of the Fermi level in the n-type $ZnSiP_2$ samples. In disagreement with the recharching model developed for the dominant native defects in $ZnGeP_2$ we could detect both Si_{Zn}^+ and V_{Zn}^- in the dark. This contradiction could be resolved by scanning surface potential microscopy measurements, which have shown that the Fermi level position laterally varies in these samples, realizing the paramagnetic states of both defects in different regions of the sample.
© 2003 Elsevier B.V. All rights reserved.

Keywords: $ZnSiP_2$; Native point defects; EPR; Electrical properties

1. Introduction

The ternary II–IV–V_2 semiconductors are promising for high-power optical frequency-conversion applications in the near and mid-infrared region. Their potential for nonlinear optical (NLO) applications has been studied during the last decades [1–5]. For such applications the crystals must have a high single crystal quality, high NLO coefficients with an appropriate birefringence and a large transparent wavelength range. While zinc germanium diphosphide ($ZnGeP_2$) is an established NLO material in the 0.7–12 μm wavelength region [5], the direct use of $ZnSiP_2$ for such frequency-conversion applications is quite restricted. The substitution of Ge by Si reduces not only the second-order susceptibility [4], but also, of particular relevance, the birefringence to very small values [6,7], making phase matching above a larger wavelength region very difficult. Nonetheless, the development of optically confined birefringent chalcopyrite heterostructures favors at present the system $ZnGeP_2$–$ZnSiP_2$ lattice-matched on GaP or Si substrate [8]. Some II–IV–V_2 compounds like $CdGeP_2$ and $ZnGeP_2$ are also viable candidates for future spintronic

*Corresponding author. Tel.: +49-30-314-26601; fax: +49-30-314-22569.

E-mail address: gehlhoff@sol.physik.tu-berlin.de (W. Gehlhoff).

[1] Leave from the Ioffe Physico-Technical Institute, RAS, 194021 St. Petersburg, Russia.

0921-4526/$ - see front matter © 2003 Elsevier B.V. All rights reserved.
doi:10.1016/j.physb.2003.09.201

devices because of their ferromagnetic behavior at room temperature when heavily doped with Mn [9]. At present, many of the optical and electrical properties of $ZnSiP_2$ are obviously dominated by native and impurity defects introduced unintentionally during growth. However, in contrast to the knowledge on such defects and their energy level positions in the band gap in $ZnGeP_2$, essentially nothing is known on these defects in $ZnSiP_2$ [10]. For both infrared frequency conversion and spintronic application the native and impurity defects have to be minimized and, in turn, controlled n- and p-type behavior must be achieved.

The main focus of the present $ZnSiP_2$ study is the characterization of the intrinsic defects by electron paramagnetic resonance (EPR) as well as of the strong potential variations detected for different sample region by scanning surface potential microscopy (SSPM) measurements.

2. Experimental details

The deep-red transparent $ZnSiP_2$ bulk crystals used in this work were grown by gas phase transport. The crystals show a needlelike habit along a $\langle 1\,1\,1 \rangle$ axis with $\{1\,0\,1\}$ and $\{1\,1\,2\}$ facets parallel to the axis. The EPR and photo-EPR measurements were carried out using a Bruker ESP 300E spectrometer operating at the X-band ($\nu \cong 9.5$ GHz) and Q-band ($\nu \cong 34$ GHz). Temperatures in the range of 3.9–300 K were achieved with Oxford Instruments continuous flow cryostats. The samples could be optically excited by monochromatic or filtered light [11]. To avoid the cutting of the small samples we used the growth facets and special sample holders to realize the magnetic field rotation in the different crystallographic planes.

Tapping mode atomic force microscopy (AFM) in conjunction with SSPM measurements were performed to visualize simultaneously the surface morphology and the corresponding potential distribution of different facets of $ZnSiP_2$. In absence of localized coulomb charges, the measured SSPM signal is equal to the surface potential of the layer, which is mapped over the sample surface with a spatial resolution in submicron scale. Its magnitude reflects the contact potential difference between the layer and the silicon tip, i.e. the difference in the work functions of both materials. That is sensitive to carrier concentration gradients as well as to chemical inhomogeneities due to cluster formation [12,13]. The SSPM results were verified by scanning capacitance measurements (SCM) which probe the local C–V curve [12] in the area below the tip. In contrast to SSPM, the SCM signal is not only dependent on the carrier concentration, but also enables the separation of n- and p-type regions. The SSPM and SCM measurements were performed in a Dimension 3100 microscope with a Nanoscope IIIa controller from Digital Instruments as described elsewhere [13].

3. Experimental results and discussion

Fig. 1 shows the EPR spectrum in the X-band for the magnetic field B parallel to the c-axis of a $ZnSiP_2$ sample with the dimension $3 \times 2 \times 6\,mm^3$. These data were taken at 20 K without photoexcitation and after cooling down the sample in the dark. The middle part of the spectrum exhibits two overlapping strong signals very similar to the

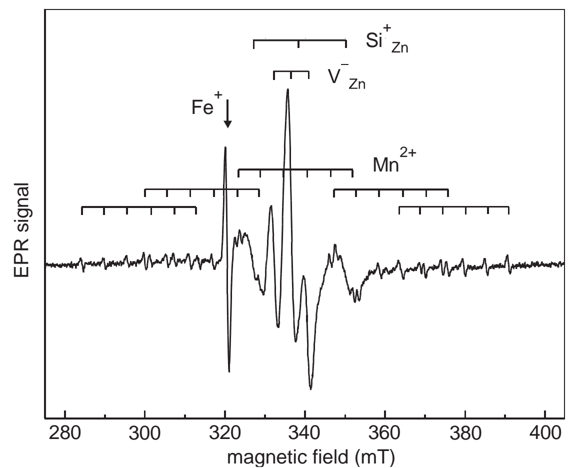

Fig. 1. X-band EPR spectrum of $ZnSiP_2$ obtained for $B \| c$ in the dark ($\nu = 9.48$ GHz, $T = 20$ K). The spectrum shows the signals from the zinc vacancy V^-_{Zn}, the anti-site center Si^+_{Zn}, and residual Mn^{2+} and Fe^+ signals described in Ref. [10].

EPR signals of the singly negatively charged zinc vacancy (V_{Zn}^{-}) [14] and the positively charged Ge at zinc site (Ge_{Zn}^{+}) in $ZnGeP_2$ [15], respectively. Besides, the EPR spectra of Mn_{Zn}^{2+} and an impurity, probably iron, with $S = \frac{3}{2}$ in a strong tetragonal crystal field are detected in this unintentional doped sample [10]. Similar to the V_{Zn}^{-} in $ZnGeP_2$ [14] the line positions of the electron spin transitions of the four crystallographic equivalent center orientations of the V_{Zn}^{-} in the tetragonal chalcopyrite crystal structure are given by the linear Zeeman interaction with $S = \frac{1}{2}$. Each electron spin transition is split into a triplet with the intensity ratio 1:2:1 by the hyperfine interaction with two equivalent phosphorus nuclei ($I = \frac{1}{2}$, 100% abundance) with a typical hyperfine line width of 2.1 mT. By fitting the Q-band line positions we obtained for $ZnSiP_2$ the principal g-values and the hyperfine interaction parameters for the two equivalent phosphorus nuclei for each of the four equivalent center orientations presented in Table 1. Small additional rotations of the hyperfine main axes around the corresponding $\langle 1\,0\,0 \rangle$ axis were neglected, because the strong overlapping of the spectrum with the residual Mn^{2+}-lines and a small misalignment of the rotation plane prevent their precise determination. Also a small rotation of the g main-axes system cannot be ruled out at present. The comparison of the g-values and the values of the hyperfine parameters between $ZnSiP_2$ and $ZnGeP_2$ presented in Table 1 indicates that the electronic wave functions of the V_{Zn}^{-} in both chalcopyrites are very similar.

The other observed triplet set of lines with intensity relation 1:2:1, which is very similar to the Ge_{Zn}^{+} in $ZnGeP_2$, can be assigned to the corresponding Si anti-site Si_{Zn}^{+}. The observed triplet structure shown in Fig. 1 for $B \| c$ is caused by a small anisotropic hyperfine interaction with two adjacent ^{31}P nuclei. As the magnetic field was rotated away from the c-axis, the hyperfine line width varied from 4.5 to 4.1 mT. The low-temperature spectrum shows a weak tetragonal distortion and its complete angular dependence can be described with $S = \frac{1}{2}$ and the g and hyperfine parameter given in Table 2. A comparison with the corresponding values for $ZnGeP_2$ [15] shows that the replacing of Ge by Si reduces the spin density at these P nuclei to 78%. The simultaneous observation of the EPR spectra V_{Zn}^{-} and Si_{Zn}^{+} without illumination is contrary to the detection of V_{Zn}^{-} and Ge_{Zn}^{+} in $ZnGeP_2$. In this material either V_{Zn}^{-} or Ge_{Zn}^{+} can be observed in the dark depending on the Fermi level position [11,16]. The recharging levels for both defects in the band gap can explain this behavior. Shifting the Fermi level in p-type $ZnGeP_2$ crystals towards the conduction band causes the recharging of the V_{Zn}^{-} to the non-paramagnetic state V_{Zn}^{2-} ($E_{opt} = E_C - 1.02\,eV$) and no V_{Zn}^{-}-related EPR signals are observed. The recharging level of the non-paramagnetic Ge_{Zn}^{2+} to the paramagnetic $Ge_{Zn}^{+}$was determined at $E_{opt} = E_v + 1.70\,eV$ and for the Fermi level at or above this energy the Ge_{Zn}^{+}-related EPR signals are observed in the dark [11,16]. Because $ZnGeP_2$ and $ZnSiP_2$ both have similar band structures and band gaps [17], it is difficult to understand the different behavior of the anti-site Si_{Zn}^{+} in $ZnSiP_2$, if we assume not quite different energy level positions for these native defects in both crystals. Studying all available samples by EPR we found different behavior concerning the detection of both defects. While some samples

Table 1
The g-values and hyperfine parameters (in $10^{-4}\,cm^{-1}$) of the zinc vacancy V_{Zn}^{-} in $ZnSiP_2$ and $ZnGeP_2$

$ZnSiP_2$		$ZnGeP_2$		Principal axes of defect site			
g	A	g	A				
2.0032	48	1.997	48	[1 0 $\bar{1}$]	[1 0 1]	[0 1 1]	[0 $\bar{1}$ 1]
2.0054	39	2.021	31	[0 1 0]	[0 1 0]	[1 0 0]	[1 0 0]
2.0196	32	2.074	33	[1 0 1]	[$\bar{1}$ 0 1]	[0 1 $\bar{1}$]	[0 1 1]

Table 2
The g-values and hyperfine parameters (in $10^{-4}\,cm^{-1}$) of the group IV anti-site defects Si_{Zn}^{+} and Ge_{Zn}^{+}in $ZnSiP_2$ and $ZnGeP_2$, respectively

$ZnSiP_2$: Si_{Zn}		$ZnGeP_2$: Ge_{Zn} [15]		Axis
g	A	g	A	
2.005	102	2.0026	167.3	$\perp c$
2.0026	107.5	2.0026	176.7	$\| c$

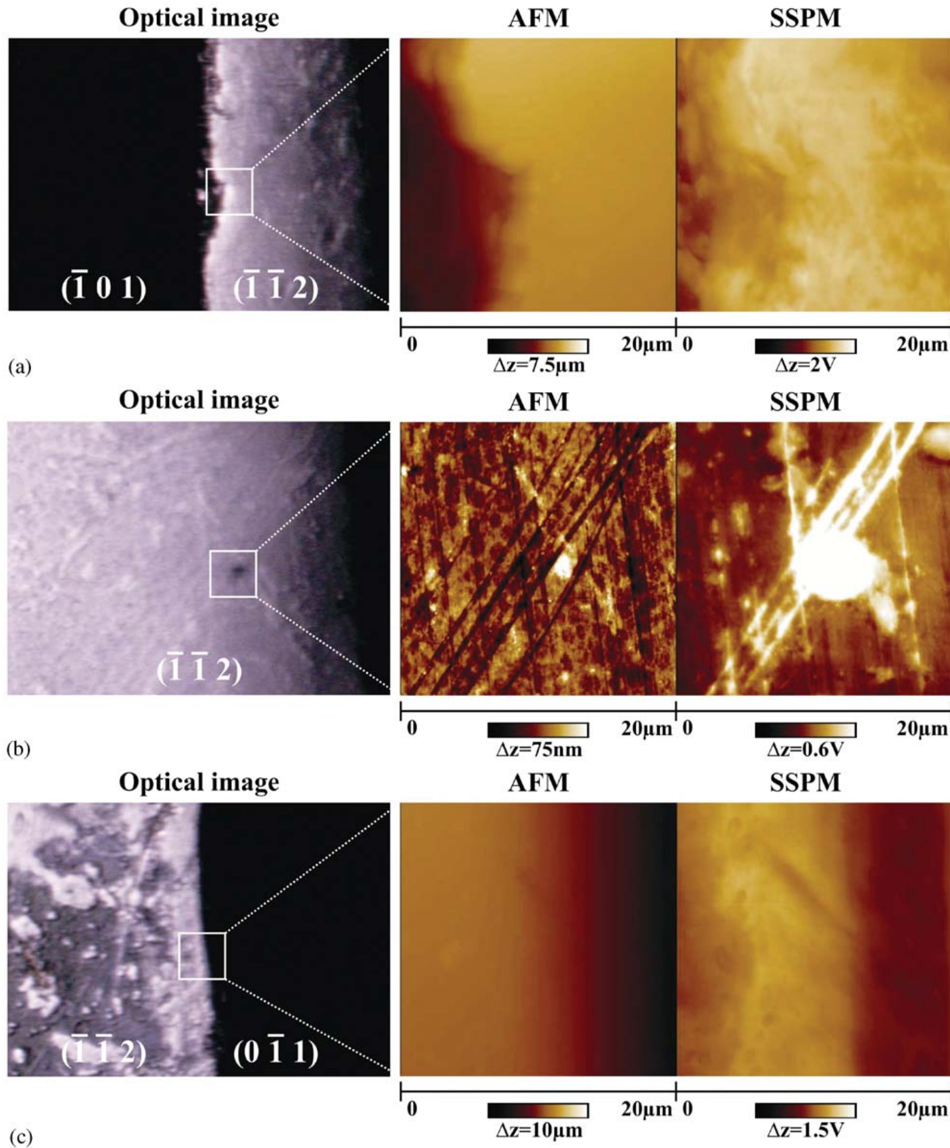

Fig. 2. Optical, AFM and corresponding SSPM images (from left to right) for the sample with the EPR spectrum shown in Fig. 1. The images are taken at the transition region from the ($\bar{1}$ 0 1) to the ($\bar{1}$ $\bar{1}$ 2) facet (a), at a typical position on the ($\bar{1}$ $\bar{1}$ 2) surface (b), as well as at the transition from the ($\bar{1}$ $\bar{1}$ 2) to the (0 $\bar{1}$ 1) facet (c), respectively.

shows the behavior described above or only the Si^{+}_{Zn} EPR spectrum [18], we also observed the same behavior for $ZnGeP_2$. To clarify the problems, we performed detailed SSPM measurement on the different facets of a $ZnSiP_2$ sample, which simultaneously showed the EPR signal of both defects in the dark. Its SSPM image shown in Fig. 2 reveals a potential drop at the transition from the ($\bar{1}$ $\bar{1}$ 2) to the ($\bar{1}$ 0 1) and to the (0 $\bar{1}$ 1) facet, respectively. These lower potential signals are due to a shift of the Fermi level towards the conduction band originated by a higher carrier concentration at the side facets. SCM maps of the same regions (not shown here) also monitor these

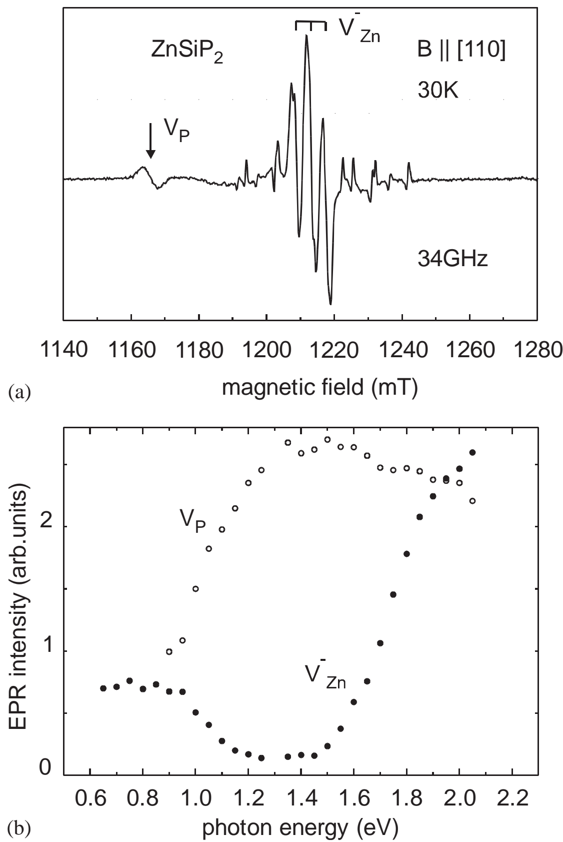

Fig. 3. Q-band EPR spectra obtained for $B \| [1\,1\,0]$ (a) and spectral dependence of the photo-induced changes of the EPR signal intensity of the V_{Zn}^- and neutral donor (V_P^0) in $ZnSiP_2$ (b) ($\nu = 34.2\,GHz$, $T = 30\,K$). (Residual Mn^{2+}-signals and a weak Mn^{2+}-background signal from the cavity overlap the V_{Zn}^-spectrum).

carrier concentration gradients strongly supporting this interpretation. For all three facets of the sample only SCM signals of n-type character were obtained without any signal due to p-type islands. In a more detailed analysis of the distinct facets we observed laterally distributed potential variations as shown in Fig. 2b for the $(\bar{1}\,\bar{1}\,2)$ region. These inhomogeneities are strongly localized and may be understood in terms of chemical non-stochiometries along the distinct surfaces. Consequently, the simultaneous detection of the V_{Zn}^-- and Si_{Zn}^+-related EPR spectra in some $ZnSiP_2$ samples can be explained by a strong variation of the Fermi level position across the sample.

Similar to $ZnGeP_2$ we could find the EPR signal from the phosphorus vacancy V_P^0 in $ZnSiP_2$ only by photo-excitation. Fig. 3 displays the spectrum and the spectral dependence of its signal intensity for a sample which show only the V_{Zn}^- EPR spectrum in the dark. The presentation establishes that similar to $ZnGeP_2$ the increase of the V_P^0 signal is accompanied with a corresponding decrease of the V_{Zn}^- signal intensity suggesting similar energy level positions of these centres in $ZnSiP_2$. Details of this study will be published elsewhere.

4. Conclusion

The present EPR study reveals three dominant native defects in $ZnSiP_2$. Similar to $ZnGeP_2$ they are the zinc (V_{Zn}) and phosphorus (V_P) vacancy as well as the group IV anti-site on Zn site Si_{Zn}(Ge_{Zn}). Because the n-type nature of the highly compensated $ZnSiP_2$ crystals, the Si_{Zn}^+ can be observed in these samples without illumination in contrast to the detection of Ge_{Zn}^+ in the highly compensated p-type $ZnGeP_2$ crystals. The simultaneous EPR detection of the V_{Zn}^- and Si_{Zn}^+ in same samples is explained by the variation of the Fermi level position across the sample as monitored by SSPM measurements.

Acknowledgements

The authors are indebted to S. Unterricker for providing the $ZnSiP_2$ crystals. This work was partially supported by the BMBF under grant 05 KK 1KTA/4, which is gratefully acknowledged.

References

[1] J.L. Shay, J.H. Wernick, Ternary Chalcopyrite Semiconductors: Growth, Electronic Properties, and Applications, Pergamon Press, Oxford, New York, 1975.

[2] H. Bondriot, E. Buhrig, H. Oettel, H.G. Schneider, II–IV–V_2-Halbleiter, in: K. Unger, H.G. Schneider (Eds.), Verbindungshalbleiter, Akademische Verlagsgesellschaft, Leipzig, 1986, pp. 339–391.

[3] K.L. Vodopyanov, F. Ganikhanov, J.M. Maffetone, I. Zwieback, W. Ruderman, Opt. Lett. 25 (11) (2000) 841.
[4] S.N. Rashkeev, S. Limpijumnong, W.R.L. Lambrecht, Phys. Rev. B 59 (1999) 2737.
[5] M.C. Ohmer, R. Pandey, Mater. Res. Bull. 23 (7) (1998) 16.
[6] G.A. Ambrazyavichuys, G.A. Babonas, A.Yu. Shileika, Lit. Fiz. Sb. (USSR) 17 (2) (1977) 205.
[7] H. Bondriot, B. Foeller, H.A. Schneider, Phys. Stat. Solidi (a) 30 (1975) K121.
[8] N. Dietz, F.L. Madarasz, Mater. Sci. Eng. B97 (2003) 182.
[9] K. Sato, G.A. Medvedkin, T. Ishibashi, S. Mitani, K. Takanashi, Y. Ishida, D.D. Sarma, J. Okabayashi, A. Fujimoro, T. Kamatani, H. Akai, J. Phys. Chem. Sol. 64 (2003) 1461.
[10] W. Gehlhoff, D. Azamat, A. Hoffmann, Mater. Sci. Semicond. Process. (Elsevier) (2003), in press.
[11] W. Gehlhoff, R.N. Pereira, D. Azamat, A. Hoffmann, N. Dietz, Physica B 308–310 (2001) 1015.
[12] D. Bonnell (Ed.), Scanning Probe Microscopy and Spectroscopy, Wiley, New York, 2001.
[13] A. Krtschil, A. Dadgar, A. Krost, J. Cryst. Growth 248 (2003) 529;
A. Krtschil, A. Dadgar, A. Krost, Appl. Phys. Lett. 82 (14) (2003) 2263.
[14] M.H. Rakovsky, W.K. Kuhn, W.J. Lauderdale, L.E. Halliburton, G.J. Edwards, M.P. Scripsick, P.G. Schunemann, T.M. Pollack, M.C. Ohmer, F.K. Hopkins, Appl. Phys. Lett. 64 (1994) 1615.
[15] S.D. Setzler, N.C. Giles, L.E. Halliburton, P.G. Schunemann, T.M. Pollak, Appl. Phys. Lett. 74 (1999) 1218.
[16] W. Gehlhoff, D. Azamat, A. Hoffmann, N. Dietz, J. Phys. Chem. Sol. 64 (2003) 1923.
[17] A. MacKinnon, Numerical Data and Functional Relationships in Science and Technology, in: O. Madelung (Ed.), Landoldt-Börnstein New Series, Group III, Vol. 17(Part h), Springer, Berlin, 1985, p. 9.
[18] W. Gehlhoff, D. Azamat, unpublished.